Contents lists available at ScienceDirect

Journal of Materiomics

journal homepage: http://ees.elsevier.com

Raman spectra and vibrational analysis of $CsPbI_3$: A fast and reliable technique to identify lead halide perovskite polymorphs

Jessica Satta [a], Claudio Melis [a], Carlo Maria Carbonaro [a], Andrea Pinna [b], Manuel Salado [c], Daniel Salazar [c], Pier Carlo Ricci [a,*]

[a] Department of Physics, University of Cagliari, S.p. No. 8 Km 0.700, 09042, Monserrato, CA, Italy
[b] Department of Mechanical, Chemical and Materials Engineering, CINSA, INSTM, University of Cagliari, Via Marengo 2, Cagliari, I-09123, Italy
[c] BCMaterials, Basque Center for Materials, Applications and Nanostructures, UPV/EHU Science Park, 48940, Leioa, Spain

ARTICLE INFO

Article history:
Received 7 July 2020
Received in revised form 31 July 2020
Accepted 11 August 2020
Available online xxx

Keywords
Raman spectroscopy
$CsPbI_3$
Inorganic lead halide perovskites
Phase transformation]

ABSTRACT

A major issue in the development of Lead halide perovskites is the assessment of the crystal structure of the samples, due to their typically limited time-stability, and the understanding of the role of external factors that can induce a crystal phase transformation (such as humidity, intense light flux, temperature, etc.). In this perspective, it is of utmost importance to have at disposal a fast and reliable experimental tool able to give an immediate indication of the polymorph of the sample with the possibility to integrate in-situ measurements for constant monitoring. In this paper we propose Raman spectroscopy as the ideal technique to solve this problem. The vibrational analysis of $CsPbI_3$ in the α-phase and δ-phase and of the Cs_4PbI_6 secondary phase is reported and all the vibrational modes are assigned by comparing experimental spectra of the phases to Raman modes calculated within the DFT framework. Finally, the mechanism of laser induced phase degradation was studied using in-situ Raman measurements providing new insights on the secondary phase generated during the process.

1. Introduction

Lead Halide organic-inorganic perovskites and, more recently, fully inorganic perovskites have attracted great attention for their excellent optical and optoelectronic properties, ranging from the tunability of the optical bandgaps to high carrier mobility and high absorption coefficients as well as long charge-carrier diffusion length[1–3]. All these properties make the $CsPbX_3$ (X = I, Br, Cl) class of Lead Halide perovskites very promising materials for different applications, like photovoltaics, phosphors and LED [2,4,5].

However, real applications of such materials are hindered by the low long-term stability of the final compounds [6,7]. Indeed, $CsPbX_3$ perovskites crystallize in four different structures: cubic phase (α), tetragonal phase (β), orthorhombic phase (γ), and orthorhombic phase (δ), but only the cubic phase possesses the suitable optical properties mentioned above. On the other hand, at room temperature α-$CsPbI_3$ is not thermodynamically stable and a temperature above 320 °C is required to set and keep this phase under controlled conditions, being the α-phase very quickly transformed into the δ-phase under ambient conditions. Thermal treatments, high flux illumination, humidity, further affect the stability of the α– phase and represent the bottleneck that prevents its exploitation in technological devices [6].

It is well known that ABX_3 perovskites are stabilized by a few cations, according to the rule of tolerance factor t:

$$t = \frac{(r_A + r_X)}{\sqrt{2}\,(r_B + r_x)}$$

where r_A r_B r_X represent the ionic sizes of the elements. A cubic structure of perovskite materials has a suitable t value ranging from 0.9 to 1.0. This value is of about 0.81 for $CsPbI_3$, thus generating an intrinsic instability in the structure [6]. However, different strategies have been tested and applied to extend the time stability of the α-$CsPbI_3$ phase at room temperature. One of them regards the doping of the structure with Rb in the A site [8], Sn, Ti, Mn in the B site [9,10] and Cl and/or Br in the anion X site [11,5]. Other strategies consist in engineering the surface to reduce the effects of water and humidity in ambient conditions, so that additives were added to the synthesis procedure to reduce the surface energy or to coat the surface and passivate it [12–15].

Finally, great efforts have been devoted to decrease the crystal dimensions to obtain active films, since a higher phase stability was observed when decreasing the grain dimensions down to nanoscale. In particular, samples of α-$CsPbI_3$ were kept stable for months when the dimensions were reduced to Quantum Dots [2,16]. However, the synthesis procedure requires tricky steps, due to the care of the sam-

Peer review under responsibility of The Chinese Ceramic Society.
* Corresponding author.
E-mail address: carlo.ricci@dsf.unica.it (P.C. Ricci)

https://doi.org/10.1016/j.jmat.2020.08.004
2352-8478/

ples and the high degree of control of the atmospheric conditions. Indeed, the synthesis should be carried out in absence of humidity (dry air), or under Nitrogen or Argon pressure, and the sample must be enveloped in a thoroughly resistant, transparent, hydrophobic material to prevent phase deterioration.

As a consequence, the control and the structural characterization take on a great importance for a deeper development of perovskites-based devices and new synthesis methods, calling for a fast and reliable in-situ crystal characterization.

The analysis of XRD pattern is certainly the most common technique applied to assess the crystal phase of the synthesized samples, but it cannot be performed in-situ for a direct control of the synthesis procedure. In addition, since in general it requires a quite long procedure and the careful preparation of the samples, it can give low information of the effective time stability, in particular during the synthesis steps, when an effective control is mostly required.

Other strategies for in-situ monitoring involve optical characterizations like luminescence and/or optical absorption measurements. Indeed, the α-phase has a lower band gap as compared to the δ phase (1.7 eV vs 2.8 eV in $CsPbI_3$, respectively) and displays a different luminescence emission peak (700 nm vs 550 nm in $CsPbI_3$) and emission efficiency [17,18]. However, these measurements give indirect information on the structure and cannot be useful, for example, in case of mixed phases.

Raman spectroscopy could be a reliable tool that conjugates the fast-experimental set-up of the optical characterization with precise structural information, useful for in-situ monitoring of phase transformations [19–21]. Nevertheless, up to now it is not a very common technique for the characterization of Lead Halide perovskites because of the difficulty in the assignment of the Raman bands. Indeed, there are a few papers that exploit Raman spectra to assess the structure achieved during the synthesis [22–26]. However, there is still disagreement on the assignment of the Raman peaks to a specific phase and no dedicated works were performed for a fully understanding of the vibrational analysis. Xiang et al. claimed that a peak at 238 cm^{-1} can be used as fingerprint for the presence of the α-phase in $CsPbI_3$ [22], and Strauss et al. identified an additional band at about 90 cm^{-1} [24]. However, both the peaks were assigned to pure PbI_2 in a different work [23]. Similarly, Raman measurements were exploited to follow the temperature-induced phase transition, identifying several bands in the low frequency part of the Raman spectrum as related to the α-phase in $CsPbI_3$ [25], but Uliel et al. demonstrated, by microcavity enhancement Raman measurements on the δ-phase, that the same bands could be related to weak van der Waals interactions between corner I—Pb—I atoms with Cs ones [26].

In this paper we would provide a definitive assignment of the Raman peaks with a careful analysis of the vibrational modes for the cubic and the orthorhombic phase of ABX_3 perovskites, carried out by experimental measurements on $CsPbI_3$ samples corroborated by DFT calculations.

Finally, we report the optically induced degradation process and we follow the phase transition of the perovskite sample by coupled in-situ luminescence and Raman measurements, providing new insights on the mechanism formation of secondary phases.

Summarizing, with this paper we would promote the Raman spectroscopy as a useful tool for the assessment of the relationships among structure, properties, and performance of Lead Halide perovskite materials.

2. Experimental

2.1. Materials

Caesium iodide (CsI, 50 ppm alkali metals, 99,9%) was purchased from Alfa-Aesar, Lead iodide (PbI_2, 99%) was purchased from Sigma Aldrich. All chemicals were used without any further purification.

2.2. Synthesis

The $CsPbI_3$ and Cs_4PbI_6 samples were synthesized by a solid-state reaction of CsI and PbI_2. Stoichiometric raw materials were weighed, grounded in an agate mortar, and then sintered in a furnace.

$$CsI + PbI_2 \rightarrow CsPbI_3$$

$$4CsI + PbI_2 \rightarrow Cs_4PbI_6$$

The stability is affected by oxygen and moisture, so the syntheses were performed under continuous vacuum conditions (experimental chamber pressure $\sim 8 \times 10^{-5}$ mbar). The samples were thermally treated at 400 °C, using a warming ramp of 10 °C/min, for 10 min and 5 h for the $CsPbI_3$ and the Cs_4PbI_6, respectively. Then, the samples were slowly cooled to room temperature.

2.3. Characterization

X-ray diffraction patterns at room temperature were collected by using a Rigaku Miniflex II diffractometer with θ-2θ Bragg-Brentano geometry with Cu Kα (λ = 1.5418 Å) radiation at room temperature. The powder patterns were recorded in the 5° ≤2θ ≤ 45° range. High temperature measurements were performed with a Bruker D8 Advance diffractometer operating at 30 kV and 20 mA, equipped with a Cu tube (λ = 1.5418 Å), a Vantec-1 PSD detector, and an Anton Parr HTK2000 high-temperature furnace. The powder patterns were recorded in the 21° ≤2θ ≤ 45° range. To avoid the evaporation of the powder at high temperature, the sample was sealed in Kapton.

Raman measurements were carried out in backscattering geometry by exciting the samples at 532 nm with a wavelength stabilized diode module (LASOS – GLK series-532) coupled with a Reflecting Bragg Grating (Optigrate-Braggrade 532) to narrow the laser line. Measurements were performed at room temperature with a triple spectrometer Jobin-Yvon Dilor integrated system with a spectral resolution of about 1 cm^{-1}. Spectra were recorded in the Stokes region by a 1200 groove/mm grating monochromator and a liquid N-cooled charge coupled device (CCD) detector system.

Steady-state photoluminescence measurements were performed with 405 nm laser excitation (Ondax LM-405-PLR-40-1) coupled with an optical fiber to an Avantes Sensilne Avaspec-ULS-TEC Spectrometer. The measurements were acquired with 1 s time window in a 300–800 nm spectral range.

The absorption measurements were obtained by diffuse reflectance spectroscopy utilizing a UV–Vis–NIR Agilent Technologies Cary 5000. Measurements were performed by using a PbS solid state photodetector using KBr as reference. The reflection configuration measures the diffuse reflection of sample with respect to a reference sample which is considered to have a 100% reflectivity. The Kubelka-Munk equation was applied to calculate the absorption properties.

Density-functional theory (DFT) calculations were carried out using Quantum Espresso [27], an integrated suite of open-source computer codes for electronic-structure calculations and material modelling based on density-functional theory, plane waves, and pseudopotentials. We used the generalized gradient approximation (GGA) in the Perdew–Burke–Ernzerhof version [28] for the exchange correlation potential and norm-conserving Troullier-Martins pseudopotentials [29].

The electronic Kohn– Sham wave functions were expanded using a plane wave basis set, up to a kinetic energy cut-off of 70 Ry. As for the k-points, we considered an 8 × 8 × 8 mesh of points distributed according to the Monkhorst–Pack algorithm within the first Brillouin zone of the reciprocal lattice. We calculated the Raman and IR spectra using Density Functional Perturbation Theory (DFPT) [30] [31], as implemented in the Quantum-Espresso package.

2.4. Crystal structure and vibrational analysis

Four crystal phases are expected in the case of $CsPbI_3$: a black cubic phase (called α), a tetragonal one (β) and two orthorhombic polymorphs (γ phase and a non-perovskite yellow δ-phase). After heating the samples above 320 °C, the room temperature yellow phase (δ-phase) converts to the black α-phase, but when cooling back to room temperature the α polymorph doesn't return immediately to its original yellow phase [32].

The α-phase is a perovskite structure, belonging to the space group number 221, *P m*-3m in the Hermann-Mauguin notation and O_h^1 in the Schönflies notation, with Z = 1. The cubic $CsPbI_3$ perovskite can be described as consisting of I^- ions corner-shared by two $[PbI_6]^{4-}$ octahedra, with the Cs cation occupying the 12-fold coordination site formed in the middle of the cube of eight octahedra. Cs atoms are in Wyckoff position *1a,* Pb atoms in 1b, and I atoms in *3c*. Caesium and lead atoms occupy O_h sites, and the three iodine atoms lie in D_{4h} sites. Each ion in O_h gives rise to T_{1u} symmetry modes, and the three iodine atoms contribute with $2T_{1u} + T_{2u}$ modes [33]. The total reducible representation at the center of the Brillouin zone is $\Gamma = 4T_{1u} + T_{2u}$. One T_{1u} mode is acoustic and the others are optical modes. T_{1u} modes are IR active, T_{2u} are silent. Vibrational Raman modes are not expected for symmetry reasons.

The δ-phase is described by the space group number 62 (*Pnma*, or D_{2h}^{16}), with four formula units in the unit cell. The constituent ions, Cs^+, Pb^{2+}, I_1^-, I_2^-, I_3^- are in Wyckoff position 4c. The symmetry of each site is C_s. The contribution of each group of ions gives the reducible representation at the center of Brillouin zone $\Gamma = 10A_g + 5A_u + 5B_{1g} + 10B_{1u} + 10B_{2g} + 5B_{2u} + 5B_{3g} + 10B_{3u}$ [33]. One of B_{1u}, B_{2u}, B_{3u} is acoustic, the others are optical modes. The A_u modes are silent, B_{1u}, B_{2u}, B_{3u} are IR active, A_g, B_{1g}, B_{2g}, B_{3g} are Raman active.

To better understand the relationship between the two phases we can consider the $[PbI_6]^{4-}$ ion. To a first approximation, $[PbI_6]^{4-}$ has an octahedral structure and Fig. 1 illustrates the six vibrational modes of an octahedral XY_6 molecule: the A_{1g}, E_g, T_{2g} vibrations are Raman-active, the T_{1u} ones are infrared-active, the T_{2u} are silent [34]. The vibrational modes that are active in a molecule can be inactive when the molecule is part of a crystal. For reason of symmetry, A_{1g}, E_g, T_{2g} modes are not active in the α-$CsPbI_3$. In the orthorhombic δ-$CsPbI_3$ the octahedra do not form any longer a 3D-chain but a 1D-chain and the octahedra are distorted: this symmetry lowering activates Raman modes and induces a splitting of degenerate vibrations, as indicated in the insert in Fig. 1.

As we mentioned in the Introduction section, the Cs_4PbI_6 secondary phase can be obtained from the $CsPbI_3$ primary compound under specific circumstances. The two crystals are quite different from the structural point of view. The Cs_4PbI_6 belongs to the space group number 167 (*R-3c:H,* or D_{3d}^6), with Z = 6. The $[PbI_6]^{4-}$ octahedra are surrounded by eight Cs^+ atoms, but I^- atoms are no longer shared between two octahedra, and Cs^+ atoms occupy two different crystallographic sites. Cs atoms are in Wyckoff position *6a* and *18e*, Pb atoms in 6b and I atoms in *36f*. Caesium atoms occupy D_3 and C_2 sites, Pb atoms occupy S_6 sites, and I atoms lie in C_1 sites. The total reducible representation at the center of the Brillouin zone is $\Gamma = 4A_{1g} + 5A_{1u} + 6A_{2g} + 7A_{2u} + 10E_g + 12E_u$ [33]. One of the A_{2u} and one of E_u modes are acoustic, the others are optical modes. A_{2u} and E_u are IR active, whilst A_{1g} and E_g are Raman active.

Fig. 2a shows the sketch of $CsPbI_3$ structure, in the two phases α and δ. Fig. 2b reports the sketch of Cs_4PbI_6 structure. From the above reported analysis, it is clear that the vibrational spectra allow distinguishing the two crystals (*vide infra*).

3. Results and discussion

3.1. X-ray and optical measurements

The crystal structures were confirmed by X-ray diffraction measurements. The patterns of δ-$CsPbI_3$ and Cs_4PbI_6 were gathered at room temperature, the one of the α-$CsPbI_3$ at 400 °C. Fig. 3a reports the experimental XRD pattern and the Rietveld analysis of the yellow δ-$CsPbI_3$ sample (ICSD 27979) obtained from the synthesis of $CsI + PbI_2$. The lattice parameters obtained for this sample are $a = 9.921(2)$ Å, $b = 4.554(3)$ Å, $c = 16.86(3)$ Å, with R factors: $R_{wp} = 11.83\%$, $R_{exp} = 7.51\%$, $R_B = 9.62\%$.

The measurements at high temperature (Fig. 3b) confirm the presence of α-$CsPbI_3$, with lattice parameter $a = 6.218(1)$ Å (ICSD 161481). It is also present, in the pattern, the platinum peak at 40°, deriving from the sample-holder, and a small percentage of δ-phase. It is to be noted that the sealing Kapton, being amorphous, has a broad peak below 21°, which doesn't affect the diffraction pattern, al-

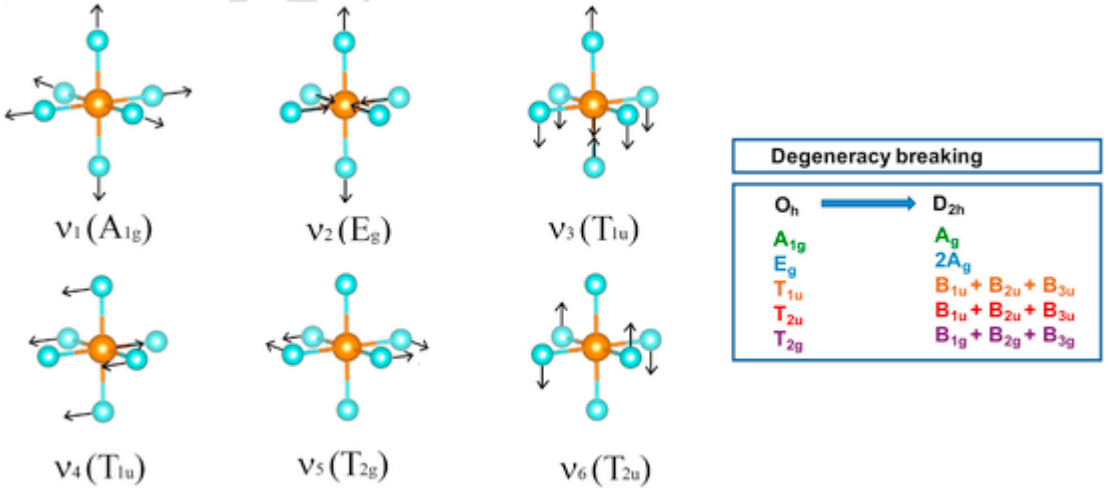

Fig. 1. Normal modes of octahedral XY_6 molecules. Conversion from O_h to D_{2h} and relative degeneracy breaking.

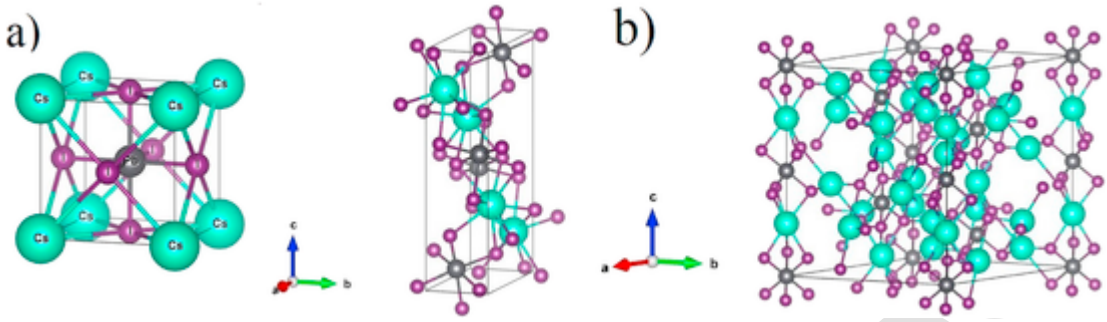

Fig. 2. a) Sketch of $CsPbI_3$ structure. On the left α-phase, on the right δ-phase. b) Sketch of Cs_4PbI_6 structure [35].

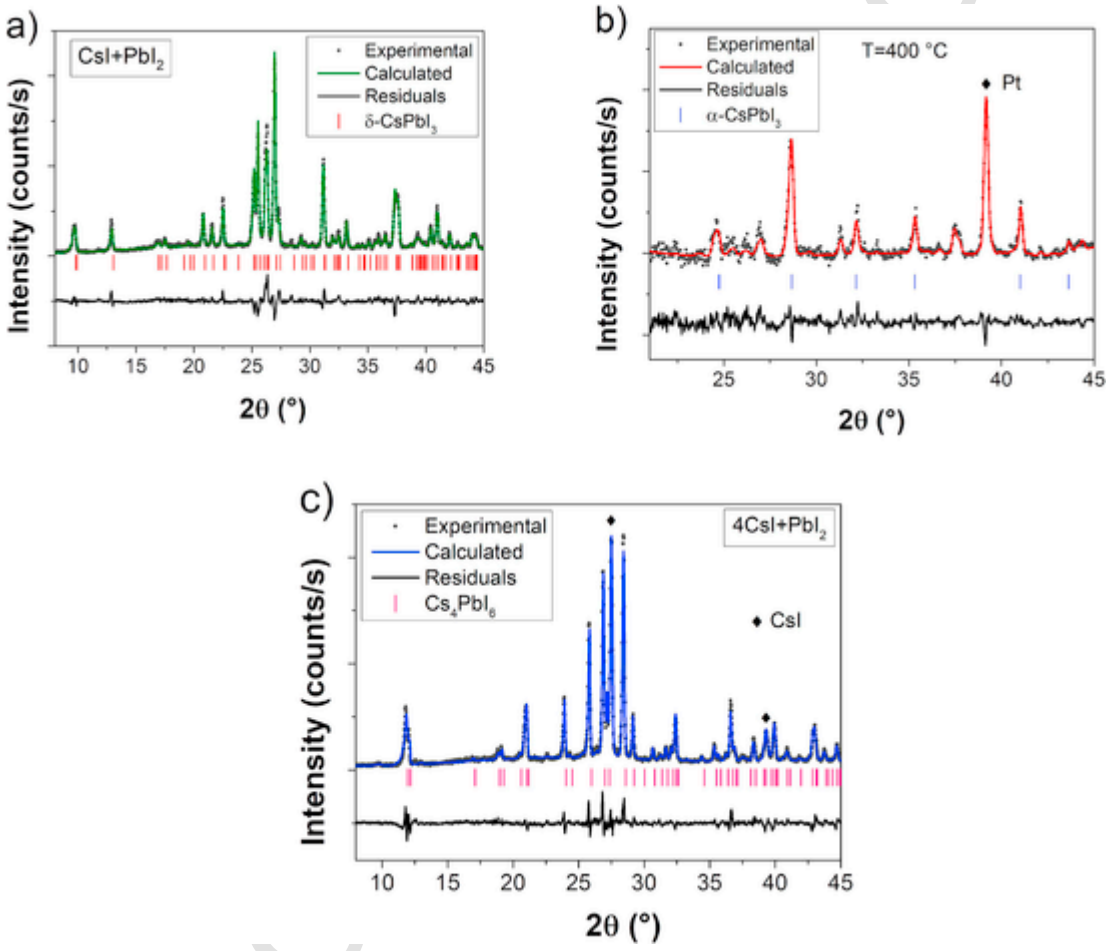

Fig. 3. a) Rietveld refinement and theoretical pattern of δ-$CsPbI_3$. b) Rietveld refinement on the measurement at high temperature and theoretical pattern of α-$CsPbI_3$. c) Rietveld refinement and theoretical pattern of Cs_4PbI_6.

though the presence of this layer has the effect of reducing the signal-to-noise ratio. For this reason, the reported pattern is a bit noisy.

In Fig. 3c it is reported the analysis of the sample deriving from the synthesis of *4CsI + PbI_2*. The pattern reveals the presence of Cs_4PbI_6 sample up to 74% by weight, with a residual contribution of CsI precursor (20%) and 6% by weight of δ-$CsPbI_3$. The lattice parameters of Cs_4PbI_6 are *a = 14.609(1)* Å, *c = 18.36(5)* Å, with R factors: R_{wp} *= 12.19%*, R_{exp} *= 7.85%*, R_B *= 9.32%*.

Fig. 4 reports the absorption and steady-state photo-luminescence spectra collected on the samples of $CsPbI_3$. The spectra confirm the success of the synthesis, showing the optical features of α and δ phases [36,37]. In particular, the former shows a highly efficient and narrow emission at 715 nm, the latter a broad and weak emission around 550 nm.

3.2. Raman measurements and simulation

For the α-$CsPbI_3$ and δ-$CsPbI_3$ structures, we considered simulation cells containing 5 and 20 atoms respectively. The initial structures obtained from single crystal data were fully optimized to the equilibrium positions with forces smaller than 0.001 eV/atom to a target pressure smaller than 0.5 kbar. The corresponding optimized lattice parameter for the cubic α-$CsPbI_3$ structure was equal to a = 6.39 Å which is identical to the value previously obtained with DFT-GGA calculations [38] and in good agreement with the experimental value obtained by X-ray measurements. For the orthorhombic δ-$CsPbI_3$ structure, the DFT lattice parameters were a = 10.73 Å, b = 4.90 Å and c = 18.24 Å, in per-

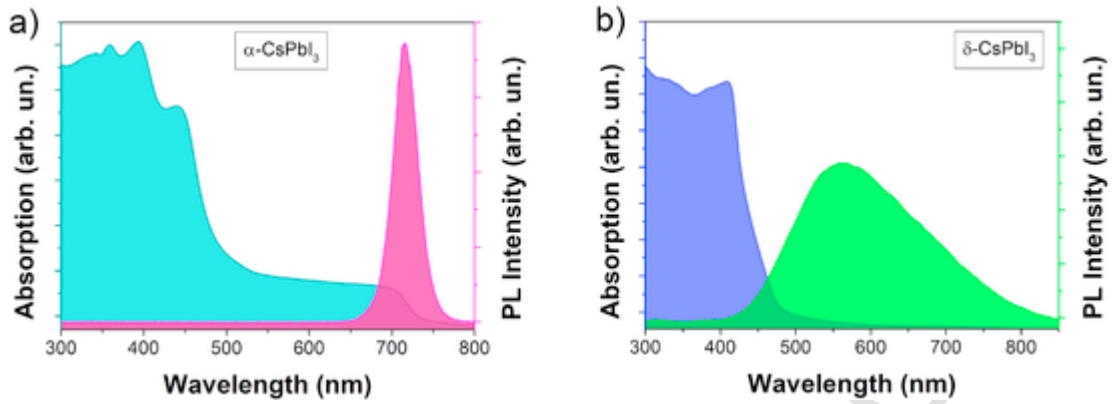

Fig. 4. a) Absorption and steady-state PL spectra of α-$CsPbI_3$ excited at 405 nm. b) Absorption and steady-state PL spectra of δ-$CsPbI_3$ excited at 405 nm.

fect agreement with previous DFT calculations [39] and in agreement with the experimental values obtained by X-ray measurements.

As already stated in the previous paragraphs, the selection rules point out that no vibrational Raman modes are allowed in the cubic α-$CsPbI_3$ for symmetry reasons and the experimental Raman spectrum, collected on the black α-phase sample, does not show any Raman features.

In Fig. 5 the experimental Raman spectrum of the sample δ-$CsPbI_3$ is reported together with the curve fitting and the vibrational modes computed by DFT simulation.

A single molecule vibrates at a well-defined frequency, but each molecule is surrounded by interacting neighbours. The observed line shape is the result of these interactions. The relaxation time from the excited state to the ground state is due to two contributions: the amplitude correlation time (τ_a), related to the single molecule, and the coherence lifetime (τ_c), related to the motion of the environment. In the case of solids, the coherence lifetime is the main contribution and the line shape has mainly a Gaussian profile. In the case of gases, coherence is easily lost and the main contribution is due to the amplitude correlation time, so that the line shape has mainly a Lorentzian profile [40]. We fitted the experimental spectrum by a multiple peak fitting procedure, with a Pseudo-Voigt function, combination of Gaussian and Lorentzian profile:

$$y = y_0 + A\left[m_u \frac{2}{\pi}\frac{w_L}{4(x-x_C)^2 + w_L^2} + (1-m_u)\frac{\sqrt{4\ln 2}}{\sqrt{\pi}w_G} e^{-\frac{4\ln 2}{w_G^2}(x-x_C)^2}\right]$$

where m_u represents the Lorentzian character of the Voigt profile, w_L and w_G are the width parameters of the Lorentzian and Gaussian components, respectively.

Eight peaks were individuated at 47, 54, 58, 65, 84, 96, 107 and 115 cm^{-1}. All the fit parameters are reported in the Supporting Information (Table S1).

As stated above, δ-$CsPbI_3$ has 30 Raman-active modes. Caesium, lead and iodide are heavy atoms, so their vibrations are expected at low Raman shifts. In particular, the Raman peaks are in the range 45–120 cm^{-1} (due to the notch filter, we cannot observe peaks at frequencies smaller than 40 cm^{-1}).

It is possible to divide the spectrum into two principal regions, around the main peaks at 54 and 107 cm^{-1} respectively. The mean distance between caesium and iodine atoms is around *3.95* Å, whilst the one between lead and iodine atoms is around *3.24* Å (ICSD 27979), indicating that the interactions between lead and iodine are stronger than the ones between caesium and iodine atoms. Therefore, it is expected that the Cs—I vibrations are located at lower frequencies with respect to the Pb—I vibrations.

DFT calculations confirm these observations and assign the main Raman features. The main vibrations are sketched in Fig. 6 and the assignation of experimental Raman peaks is reported in Table 1. The whole vibrational modes are reported in the Supporting Information (Table S2 and Figure S1). The peaks above 80 cm^{-1} mainly concern vibrations of lead and iodide atoms, whilst below 80 cm^{-1} also caesium vibrations are involved. The strongest peak at 107 cm^{-1} is assigned to a symmetric A_g mode (Fig. 6a), the shoulder at 115 cm^{-1} to an asymmetric B_{2g} mode (Fig. 6b) and the peak at 96 cm^{-1} to the convolution of two modes, A_g and B_{2g} (n. 3 and 4 in Table 1). In these modes, caesium atoms are at rest and the atoms in the $[PbI_6]^{4-}$ octahedra vibrate. The other peaks are considered as the convolution of different vibrations. The peak at 84 cm^{-1} is assigned to the convolution of four modes, B_{2g}, A_g, B_{1g} and B_{3g} (n. 5–8 in Table 1), where mainly lead and iodide atoms vibrate, whilst caesium atoms are involved in small vibrations. The peak at 64 cm^{-1} is considered the convolution of B_{1g}, B_{2g} and two A_g modes (n. 9–12 in Table 1). The peak at 47 cm^{-1} is the convolution of a A_g, B_{2g} and B_{3g} modes (n. 20, 21 and 22 in Table 1). The region around the second strongest peak, 54-58 cm^{-1}, includes wide vibrations of caesium and iodide atoms: B_{1g}, B_{2g}, B_{3g} and A_g modes (n. 13–19 in Table 1). In particular, A_g and B_{2g} modes in-

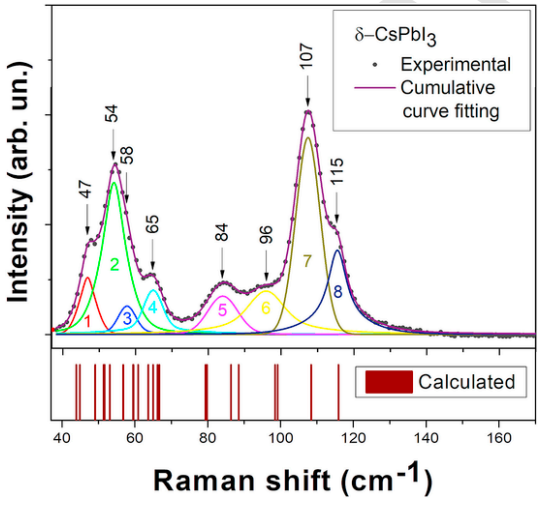

Fig. 5. Raman spectrum of δ-$CsPbI_3$, excitation 532 nm. Numbers from 1 to 8 refer to the peaks fit. For comparison the calculated modes are reported.

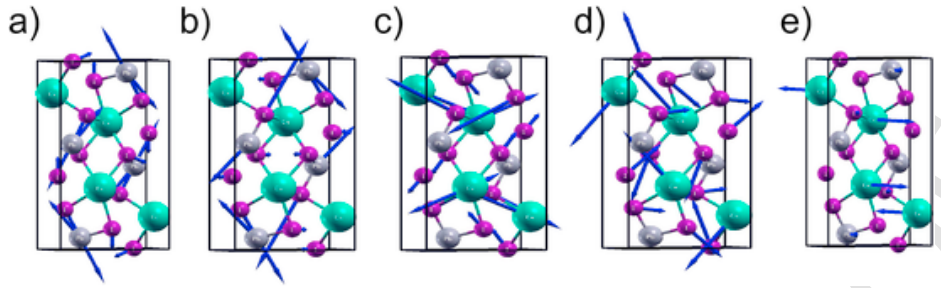

Fig. 6. Assignation of Vibrational modes. a) A_g mode, n. 2 Table 1 (107 cm^{-1}); b) B_{2g} mode, n. 1 Table 1 (115 cm^{-1}); c) A_g mode, n. 9 Table 1 (64 cm^{-1}); d) B_{2g} mode, n. 16 Table 1 (54-58 cm^{-1}); e) A_g mode, n. 17 Table 1 (54-58 cm^{-1}).

Table 1
Calculated Raman modes and assignation.

Mode number	Vibrational mode	Calculated Raman Shift (cm^{-1})	Experimental Raman shift (cm^{-1})
1	B_{2g}	115.9	115
2	A_g	108.4	107
3	A_g	99.2	96
4	B_{2g}	98.5	
5	B_{2g}	88.5	84
6	A_g	86.4	
7	B_{3g}	79.8	
8	B_{1g}	79.4	
9	A_g	66.7	64
10	B_{2g}	66.2	
11	A_g	65	
12	B_{1g}	63.7	
13	B_{2g}	60.9	54–58
14	B_{3g}	59.6	
15	B_{1g}	59.5	
16	B_{2g}	56.8	
17	A_g	53.1	
18	B_{2g}	51.7	
19	B_{3g}	51.4	
20	A_g	49.1	47
21	B_{3g}	44.9	
22	B_{2g}	43.9	

volve vibrations of Cs—I, whilst lead atoms are at rest (Fig. 6c and d), and the A_g mode in Fig. 6e regards strong vibrations of caesium.

It was already observed that a high-power laser beam can degrade the stability of perovskite samples [23,41,42]. Thus, one should take care of controlling the experimental conditions in order to avoid the reported degradation when performing Raman and luminescence measurements. To perform in-situ measurements, we aligned the Raman and luminescence set-up to exploit the same microscope system to collect both the signals from the sample. Once the sample reached 320 °C and the synthesis was accomplished, the sample was placed under the microscope to collect the luminescence and Raman signal. Indeed, carrying out the Raman and photoluminescence measurements, by increasing the power of the laser, we observed an abrupt decrease in the luminescence signal (the laser density power was increased up to 955 mW/mm^2). Thanks to the previous analysis on the vibrational modes, we were able to study the degradation phenomenon by means of Raman spectroscopy.

In Fig. 7a three Raman spectra related to this process are reported, the spectra being recorded at zero irradiation time and after 10 and 30 s of laser irradiation (taking into account the short time considered we assume that the sample temperature kept almost constant). Fig. 7b reports the static luminescence measurements (excitation wavelength, 405 nm) recorded, simultaneously, with the Raman spectra.

As expected, being recorded at room temperature, the sample presents a mixed structure: the zero-irradiation time PL spectrum, taken with very small laser power density (50 mW/mm^2), indicates the presence of α-phase (at naked eye the sample appeared indeed black). On the other hand, the Raman spectrum already reveals the presence of the δ-phase. It is important to recall that the cubic α-phase doesn't generate any Raman feature and the fast phase transition from α to δ-phase at room temperature is well documented. After 10 s of irradiation,

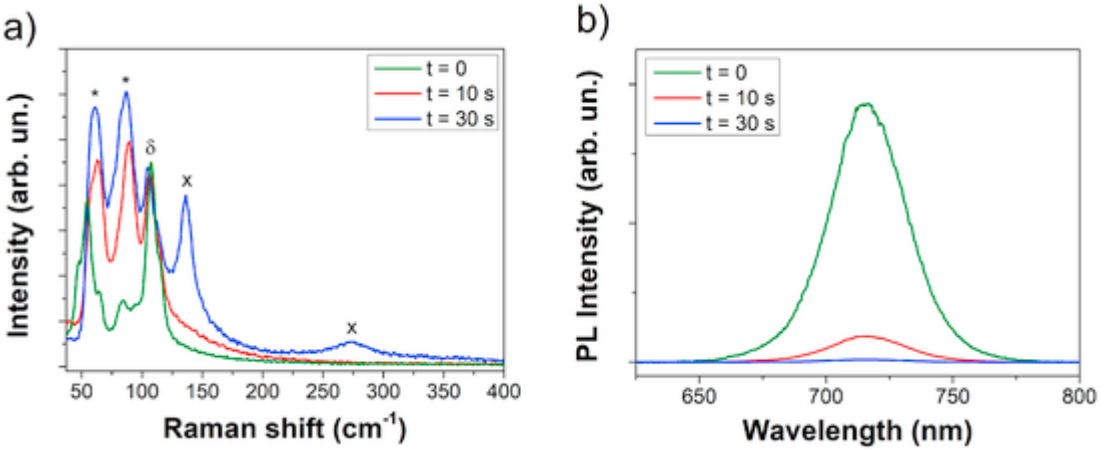

Fig. 7. a) Raman spectrum of $CsPbI_3$ after laser degradation. The main peaks of the different phases are indicated in figure: (*) Cs_4PbI_6 phase, (δ) δ-$CsPbI_3$ phase, (x) PbO. b) Luminescence collected simultaneously with the relative Raman spectrum.

the Raman signal related to the δ-phase remain constant (as suggested by the peak at 107 cm^{-1}) but two vibrational features at 65 and 90 cm^{-1} increase their relative intensity. The latter could still recall for the Raman bands related to the δ−$CsPbI_3$ phase (see Fig. 5 and Table 1), but they have different relative intensity with respect to the other bands, and, mainly, appear at slightly red-shifted positions (at 65 and 90 cm^{-1} instead of 54 and 84 cm^{-1}). We also noticed that the relative contribution of the band at 90 cm^{-1} is larger than the one of 84 cm^{-1} band in Fig. 5. As the irradiation proceeds, the 107 cm^{-1} band remains still constant, but the formation of two new peaks at 136 and 270 cm^{-1} is clearly visible. These last two peaks are assigned to lead oxide [43]. The luminescence collected simultaneously drops swiftly to zero, strongly suggesting the full degradation of the α-phase and its absence after 30 s under illumination.

In literature the synthesis process of α−$CsPbI_3$ from a secondary compound of caesium, lead and iodine, Cs_4PbI_6, is reported [12]. We hypothesize that an inverse process is activated by laser irradiation, leading from α−$CsPbI_3$ to Cs_4PbI_6:

$$4\,\alpha\ CsPbI_3 \rightarrow Cs_4PbI_6 + 3PbI_2$$

Lead iodide is unstable in ambient air under irradiation, because oxygen oxidizes the iodide with the formation of lead oxide and elemental iodine [44,45]:

$$2PbI_2 + O_2 \rightarrow 2PbO + 2I_2$$

To confirm the above considerations about the degradation process, pure Cs_4PbI_6 samples were synthesized (see Fig. 3c and the crystal sketch reported in Fig. 2b). Fig. 8 reports the Cs_4PbI_6 Raman spectrum, characterized by two main peaks at 65 and 90 cm^{-1} allowing to confirm the aforementioned hypothesis, fully justifying both the spectral position and the relative contribution of the recorded bands in Fig. 7a.

In view of these results it is possible to define the experimental Raman peaks of δ−$CsPbI_3$ and Cs_4PbI_6, completing and clarifying previous works [22–26]. Further, we showed that, for symmetry reasons, α-$CsPbI_3$ doesn't have allowed Raman modes.

4. Conclusions

The vibrational analysis of lead halide perovskites in the α-phase and δ-phase is reported. The analysis allowed to completely discriminate between the two crystal phases, being the cubic α-phase lacking in allowed Raman modes, because of symmetry reasons, and the orthorhombic δ-phase characterized by several distinctive bands. Corroborated by theoretical argumentations and DFT calculations, we were able to definitely assign the experimental Raman modes in δ−$CsPbI_3$.

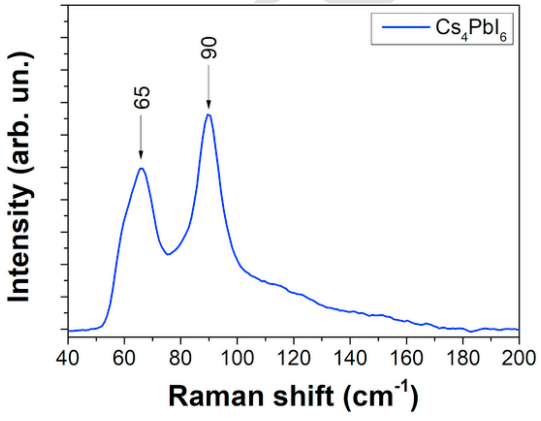

Fig. 8. Raman spectrum of Cs_4PbI_6.

Further, the analysis of the Raman modes was extended to the secondary phase, Cs_4PbI_6, allowing to successfully study, by in-situ measurements, the laser-induced phase degradation of α−$CsPbI_3$ with the formation of the secondary phase Cs_4PbI_6 and relative by-products.

Beyond the vibrational characterization, Raman spectroscopy was proven to be a fast and reliable experimental tool to characterize the different polymorphs of lead halide perovskites and to follow in-situ phase transitions or degradation processes caused by laser irradiation.

Declaration of competing interest

The authors declare that they have no known competing financial interests or personal relationships that could have appeared to influence the work reported in this paper.

5. Acknowledgments

The authors acknowledge the support of the "Fondazione di Sardegna" within the project L.R 7. CUP F74I19000930007 "NG-Light: a new generation of phosphors". Technical support provided by A. Larrañaga in SGIker (UPV/EHU, GV/EJ, ESF) is gratefully acknowledged.

Manuel Salado thanks the National Research grant "Juan de la Cierva" (FJCI-2017-31761).

Appendix A. Supplementary data

Supplementary data to this article can be found online at https://doi.org/10.1016/j.jmat.2020.08.004.

References

[1] A Bano, P Khare, V Parey, A Shukla, N K Gaur The structural, electronic and phonon behavior of CsPbI3: a first principles study. AIP Conf Proc 2016;1728. doi:10.1063/1.4946150.
[2] X Jia, C Zuo, S Tao, K Sun, Y Zhao, S Yang, et al. CsPb(IxBr1−x)3 solar cells. Sci Bull 2019;64:1532–1539. doi:10.1016/j.scib.2019.08.017.
[3] R J Sutton, G E Eperon, L Miranda, E S Parrott, B A Kamino, J B Patel, et al. Bandgap-tunable cesium lead halide perovskites with high thermal stability for efficient solar cells. Adv Energy Mater 2016;6:1–6. doi:10.1002/aenm.201502458.
[4] Q Jiang, Y Zhao, X Zhang, X Yang, Y Chen, Z Chu, et al. Surface passivation of perovskite film for efficient solar cells. Nat Photon 2019;13:460–466. doi:10.1038/s41566-019-0398-2.
[5] L Protesescu, S Yakunin, M I Bodnarchuk, F Krieg, R Caputo, C H Hendon, et al. Nanocrystals of cesium lead halide perovskites (CsPbX3, X = Cl, Br, and I): novel optoelectronic materials showing bright emission with wide color gamut. Nano Lett 2015;15:3692–3696. doi:10.1021/nl5048779.
[6] W Ke, I Spanopoulos, C C Stoumpos, M G Kanatzidis Myths and reality of HPbI3 in halide perovskite solar cells. Nat Commun 2018;9. doi:10.1038/s41467-018-07204-y.
[7] A Marronnier, H Lee, B Geffroy, J Even, Y Bonnassieux, G Roma Structural instabilities related to highly anharmonic phonons in halide perovskites. J Phys Chem Lett 2017;8:2659–2665. doi:10.1021/acs.jpclett.7b00807.
[8] Q Zhao, A Hazarika, L T Schelhas, J Liu, E A Gaulding, G Li, et al. Size-dependent lattice structure and confinement properties in CsPbI3 perovskite nanocrystals: negative surface energy for stabilization. ACS Energy Lett 2020;5:238–247. doi:10.1021/acsenergylett.9b02395.
[9] B Luo, F Li, K Xu, Y Guo, Y Liu, Z Xia, et al. B-Site doped lead halide perovskites: synthesis, band engineering, photophysics, and light emission applications. J Mater Chem C 2019;7:2781–2808. doi:10.1039/c8tc05741a.
[10] Q A Akkerman, D Meggiolaro, Z Dang, F De Angelis, L Manna Fluorescent alloy CsPbxMn1-xI3 perovskite nanocrystals with high structural and optical stability. ACS Energy Lett 2017;2:2183–2186. doi:10.1021/acsenergylett.7b00707.
[11] B T Diroll, H Zhou, R D Schaller Low-temperature absorption, photoluminescence, and lifetime of CsPbX3 (X = Cl, Br, I) nanocrystals. Adv Funct Mater 2018;28:1–7. doi:10.1002/adfm.201800945.
[12] P Luo, W Xia, S Zhou, L Sun, J Cheng, C Xu, et al. Solvent engineering for ambient-air-processed, phase-stable CsPbI3 in perovskite solar cells. J Phys Chem Lett 2016;7:3603–3608. doi:10.1021/acs.jpclett.6b01576.
[13] Q Wang, X Zheng, Y Deng, J Zhao, Z Chen, J Huang Stabilizing the α-phase of CsPbI3 perovskite by sulfobetaine zwitterions in one-step spin-coating films. Joule 2017;1:371–382. doi:10.1016/j.joule.2017.07.017.
[14] B Li, Y Zhang, L Fu, T Yu, S Zhou, L Zhang, et al. Surface passivation engineering strategy to fully-inorganic cubic CsPbI3 perovskites for high-performance solar cells. Nat Commun 2018;9. doi:10.1038/s41467-018-03169-0.

[15] B Jeong, H Han, Y J Choi, S H Cho, E H Kim, S W Lee, et al. All-inorganic CsPbI3 perovskite phase-stabilized by poly(ethylene oxide) for red-light-emitting diodes. Adv Funct Mater 2018;28:1–8. doi:10.1002/adfm.201706401.
[16] A Swarnkar, A R Marshall, E M Sanehira, B D Chernomordik, D T Moore, J A Christians, et al. Quantum dot-induced phase stabilization of α-CsPbI3 perovskite for high-efficiency photovoltaics. Science 2016;354(80):92–95. doi:10.1126/science.aag2700.
[17] J Deng, J Li, Z Yang, M Wang All-inorganic lead halide perovskites: a promising choice for photovoltaics and detectors. J Mater Chem C 2019;7:12415–12440. doi:10.1039/c9tc04164h.
[18] X Li, Y Wu, S Zhang, B Cai, Y Gu, J Song, et al. CsPbX3 quantum Dots for lighting and displays: roomerature synthesis, photoluminescence superiorities, underlying origins and white light-emitting diodes. Adv Funct Mater 2016;26:2435–2445. doi:10.1002/adfm.201600109.
[19] P C Ricci, C M Carbonaro, L Stagi, M Salis, A Casu, S Enzo, et al. Anatase-to-Rutile phase transition in TiO 2 nanoparticles irradiated by visible light. J Phys Chem C 2013;117:7850–7857. doi:10.1021/jp312325h.
[20] G Pezzotti, A A Porporati Raman spectroscopic analysis of phase-transformation and stress patterns in zirconia hip joints. J Biomed Optic 2004;9:372. doi:10.1117/1.1647547.
[21] C A Chen, Y S Huang, W H Chung, D S Tsai, K K Tiong Raman spectroscopy study of the phase transformation on nanocrystalline titania films prepared via metal organic vapour deposition. J Mater Sci Mater Electron 2009;20:303–306. doi:10.1007/S10854-008-9595-3. Springer.
[22] S Xiang, Z Fu, W Li, Y Wei, J Liu, H Liu, et al. Highly air-stable carbon-based α-CsPbI3 perovskite solar cells with a broadened optical spectrum. ACS Energy Lett 2018;3:1824–1831. doi:10.1021/acsenergylett.8b00820.
[23] K E A Hooper, H K H Lee, M J Newman, S Meroni, J Baker, T M Watson, et al. Probing the degradation and homogeneity of embedded perovskite semiconducting layers in photovoltaic devices by Raman spectroscopy. Phys Chem Chem Phys 2017;19:5246–5253. doi:10.1039/c6cp05123e.
[24] D B Straus, S Guo, R J Cava Kinetically stable single crystals of perovskite-phase CsPbI3. J Am Chem Soc 2019;141:11435–11439. doi:10.1021/jacs.9b06055.
[25] W Zhou, F Sui, G Zhong, G Cheng, M Pan, C Yang, et al. Lattice dynamics and thermal stability of cubic-phase CsPbI3 quantum Dots. J Phys Chem Lett 2018;9:4915–4920. doi:10.1021/acs.jpclett.8b02036.
[26] T Ben Uliel, L Gouda, H Aviv, A Itzhak, Y R Tischler Microcavity enhancement of low-frequency Raman scattering from a CsPbI3 thin film. J Raman Spectrosc 2019;50:1672–1678. doi:10.1002/jrs.5715.
[27] P Giannozzi, S Baroni, N Bonini, M Calandra, R Car, C Cavazzoni, et al. Quantum espresso: a modular and open-source software project for quantum simulations of materials. J Phys Condens Matter 2009. doi:10.1088/0953-8984/21/39/395502.
[28] J P Perdew, K Burke, M Ernzerhof Generalized gradient approximation made simple. Phys Rev Lett 1996. doi:10.1103/PhysRevLett.77.3865.
[29] N Troullier, J L Martins Efficient pseudopotentials for plane-wave calculations. Phys Rev B 1991. doi:10.1103/PhysRevB.43.1993.
[30] P Giannozzi, S De Gironcoli, P Pavone, S Baroni Ab initio calculation of phonon dispersions in semiconductors. Phys Rev B 1991. doi:10.1103/PhysRevB.43.7231.
[31] M Lazzeri, F Mauri First-principles calculation of vibrational Raman spectra in large systems: signature of small rings in crystalline SiO2. Phys Rev Lett 2003. doi:10.1103/physrevlett.90.036401.
[32] A Marronnier, G Roma, S Boyer-Richard, L Pedesseau, J M Jancu, Y Bonnassieux, et al. Anharmonicity and disorder in the black phases of cesium lead iodide used for stable inorganic perovskite solar cells. ACS Nano 2018;12:3477–3486. doi:10.1021/acsnano.8b00267.
[33] D L Rousseau, R P Bauman, S P S Porto Normal mode determination in crystals. J Raman Spectrosc 1981;10:253–290. doi:10.1002/jrs.1250100152.
[34] K. Nakamoto Part A: theory and applications in inorganic chemistryhttps://doi.org/10.1002/0470027320.s41042009
[35] K Momma, F Izumi VESTA 3 for three-dimensional visualization of crystal, volumetric and morphology data. J Appl Crystallogr 2011. doi:10.1107/S0021889811038970.
[36] M Lai, Q Kong, C G Bischak, Y Yu, L Dou, S W Eaton, et al. Structural, optical, and electrical properties of phase-controlled cesium lead iodide nanowires. Nano Res 2017;10:1107–1114. doi:10.1007/s12274-016-1415-0.
[37] R J Sutton, M R Filip, A A Haghighirad, N Sakai, B Wenger, F Giustino, et al. Cubic or orthorhombic? Revealing the crystal structure of metastable black-phase CsPbI3 by theory and experiment. ACS Energy Lett 2018;3:1787–1794. doi:10.1021/acsenergylett.8b00672.
[38] J Brgoch, A J Lehner, M Chabinyc, R Seshadri Ab initio calculations of band gaps and absolute band positions of polymorphs of RbPbI3 and CsPbI3: implications for main-group halide perovskite photovoltaics. J Phys Chem C 2014. doi:10.1021/jp508880y.
[39] M Maqbool, G Rehman, L Ali, M Shafiq, R Iqbal, R Ahmad, et al. Structural, electronic and optical properties of CsPbX3(X = Cl, Br, I) for energy storage and hybrid solar cell applications. J Alloys Compd 2017. doi:10.1016/j.jallcom.2017.02.147.
[40] M Bradley Curve fitting in Raman and IR Spectroscopy : basic theory of line shapes and applications. Thermo Fish Sci Appl Note 2007. doi:10.1002/2015JG003204.Received.
[41] Y Li, X Xu, C Wang, B Ecker, J Yang, J Huang, et al. Light-induced degradation of CH3NH3PbI3 hybrid perovskite thin film. J Phys Chem C 2017;121:3904–3910. doi:10.1021/acs.jpcc.6b11853.
[42] J S Niezgoda, B J Foley, A Z Chen, J J Choi Improved charge collection in highly efficient CsPbBrI2 solar cells with light-induced dealloying. ACS Energy Lett 2017;2:1043–1049. doi:10.1021/acsenergylett.7b00258.
[43] L Burgio, R J H Clark, S Firth Raman spectroscopy as a means for the identification of plattnerite (PbO2), of lead pigments and of their degradation products. Analyst 2001;126:222–227. doi:10.1039/b008302j.
[44] A J Forty Observations of the decomposition of crystals of lead iodide in the electron microscope. Philos Mag A 1960;5:787–797. doi:10.1080/14786436008241217.
[45] G Popov, M Mattinen, T Hatanpää, M Vehkamäki, M Kemell, K Mizohata, et al. Atomic layer deposition of PbI2 thin films. 2019. doi:10.1021/ACS.CHEMMATER.8B04969.S001.

Biography

Prof. Pier Carlo Ricci, Since 2010 is tenured as associate professor at the Department of Physics of the University of Cagliari. PhD in Physics in 2003 at the University of Cagliari, Invited Professor at the University of Grenoble in 2018, Universidad de Castilla-La Mancha Spain (2017), George-August University (2014). The research activity is mainly devoted to the study of the optical and structural properties of solid state systems, like nanocrystals, crystalline oxides, and hybrid system organic/inorganic.

Jessica Satta finished her master's degree in physics in 2018 at University of Cagliari, with a thesis on "Synthesis and characterization of Zinc Calcium Oxysulfide". Traineeship at Universidad de Castilla-La Mancha, in Ciudad Real, about the magnetic characterization of nanoparticles. Now, she's a PhD student in Physics at University of Cagliari, under the supervision of prof. Pier Carlo Ricci. She's working on structural and optical characterization of all-inorganic perovskites, and their phase transitions.